

Electronic Supplementary Information (ESI)

Magnetically Actuated Functional Gradient Nanocomposites for Strong and Ultra-durable Biomimetic Interfaces/Surfaces

Zhengzhi Wang, Xiaoming Shi, Houbing Huang,* Chenmin Yao, Wen Xie, Cui Huang, Ping Gu, Xingqiao Ma, Zuoqi Zhang, and Long-Qing Chen*

Experimental Section

■ Materials

Dispersed Fe₃O₄ nanoparticles (average diameter of 10 nm, oleate-stabilized in cyclohexane) prepared by the thermal decomposition method ^[s1] were purchased from Nanjing XFNANO Materials Tech Co., Ltd, China. Tetraethyl orthosilicate (TEOS), polyvinylpyrrolidone (PVP), dichloromethane (DCM), dimethylformamide (DMF), 3-trimethoxysilylpropyl methacrylate (γ -MPS), ammonium hydroxide (28 wt.% in water), diethyl ether (DE), ethanol, and toluene were purchased from Sigma-Aldrich (Milwaukee, WI, USA). Model dental resins of bisphenol A-glyceryls methacrylate (Bis-GMA) and triethylene glycol dimethacrylate (TEGDMA), along with a photoinitiator system consisting of camphorquinone (CQ) and ethyl 4-dimethylaminobenzoate (EDAB) were also purchased from Sigma-Aldrich. UV-curable polyurethane acrylate resins (PUA) consisting of urethane and acrylate prepolymers, a UV photoinitiator, a monomeric modulator, and a releasing agent were purchased from Minuta Tech. Co. Ltd. (Korea). Disk-shaped permanent NdFeB magnets (diameter of 60 mm and height of 5 mm, saturation magnetization of \sim 1.3 T) were purchased from Supermagnete (Germany). All chemicals were used as received unless otherwise specified.

■ Preparation and characterizations of silica-coated Fe₃O₄ nanoparticles (Fe₃O₄@SiO₂ NPs)

Fe₃O₄@SiO₂ NPs were synthesized based on a combination of ligand exchange and

modified Stöber method as detailed in the literature [s2]. In the first step, the commercially available oleate-stabilized Fe₃O₄ NPs were converted to PVP-stabilized NPs to modify the surface hydrophobicity. 0.5 ml of oleate-stabilized NPs in cyclohexane was diluted with 10 ml of DCM/DMF (1/1 by volume) solution, while 100 mg of PVP was added subsequently and refluxed at 100 °C for over 12 h. The mixture was then added dropwise into DE (12 ml) to form precipitate. After washing and centrifuging the precipitate, a dispersion of the PVP-stabilized Fe₃O₄ NPs was obtained by transferring the precipitate into 12 ml of ethanol solvent. In the second step, the hydrophilic PVP-stabilized NPs were silicated *via* the Stöber method [s3]. Briefly, the dispersed PVP-stabilized NPs were mixed with 0.5 ml of ammonium hydroxide and 0.1 ml of TEOS precursor diluted in ethanol (10 vol.%). The mixture was stirred overnight and centrifuged at 8000 rpm for 2 h. Afterwards, 1 ml of TEOS in ethanol (5 vol.%) was added again at a rate of 0.2 ml/h using a microliter syringe pump. After rigorous stirring over 24 h and centrifuging at 8000 rpm for 1 h, Fe₃O₄@SiO₂ NPs (SiO₂ shell thickness of ~ 5 nm, Figure 2e) dispersed in ethanol were successfully prepared. The thickness of the SiO₂ shell could be easily adjusted by varying the TEOS precursor amounts. For the current study, however, the experimental parameters given above were determined to obtain Fe₃O₄@SiO₂ NPs with average size of 20 nm (Figure 2e).

The field-dependent magnetization curves (hysteresis loops) of the bare Fe₃O₄ and Fe₃O₄@SiO₂ NPs were measured by a vibration sample magnetometer (VSM Model 7400, Lakeshore, OH, USA) with applied magnetic fields between -10 and 10 KOe at room temperature (Figure S1).

■ Preparation and characterizations of polymer nanocomposites with various filler loadings

Typical dental resins (Bis-GMA and TEGDMA) were selected as the model resin matrix and the prepared Fe₃O₄@SiO₂ NPs acted as the reinforcing fillers for the nanocomposites. Fe₃O₄@SiO₂ NPs were first dried and silanized with γ -MPS to provide

essential covalent connection between the filler and the matrix. The silanization was realized by reacting the fillers with the coupling agent in toluene at 120 °C for 6 h. After washing with toluene for several times, the silanized Fe₃O₄@SiO₂ NPs were mixed with Bis-GMA/TEGDMA (1/1 by weight, viscosity of 0.225 Pa.s) compound (including 0.2 wt.% CQ and 0.8 wt.% EDAB as the photoinitiator) in 10 vol.% increment to obtain filler contents of 0-40 vol.% (0-58.9 wt.%). The various volume fractions were converted from the corresponding weight percentages based on the respective densities of the resin matrices (1.16 g/cm³ for Bis-GMA and 1.09 g/cm³ for TEGDMA) and nanofillers (5.18 g/cm³ for magnetic core and 2.20 g/cm³ for silica shell). Fillers and resins were blended in a centrifugal mixer (DAC 150.1 FVZ-K, Hauschild & Co KG, Hamm, Germany) at 2500 rpm for 10 min to ensure sufficient mixing and uniform filler distribution. The composite mixture was then placed in a vacuum chamber for 1 h to degas bubbles inside. Following that, the mixture was poured into a Teflon mold (2.5 mm diameter and 2 mm height) and polymerized with a blue LED light (LZ1-00DB00, LED Engin Inc., San Jose, CA, USA). The light irradiation (1000 mW/cm² for 40 s) was controlled by a LabView program through a LED/temperature controller (6340 ComboSource, Arroyo Instrument, San Luis Obispo, CA, USA). All experiments involving photo-irradiation in this study were conducted under a yellow light environment to minimize premature photopolymerization and at room temperature.

During the photopolymerization process, a remote transmission near infrared (NIR) spectrometer (NIRQuest512-2.2, Ocean Optics, Inc., Dunedin, FL, USA) configured by optical-fiber cables was used to monitor the polymerization kinetics at an integration time of 100 ms as detailed in our previous study (Figure S2) ^[s4]. After the samples were completely cured, ultrathin sections of the composites with various filler contents were made using a cryoultramicrotome (Leica EM FC7, Germany) and the distributions of the nanofillers inside the polymer matrix were examined by a Transmission Electron Microscope (TEM, Jeol EM-2100, Japan). The samples were also polished smooth and nanoindentation tests (Berkovich

tip with 100 nm tip radius, maximum load of 8000 μN , Hysitron TI 950 TriboIndenter system, Hysitron Inc., Minneapolis, MN, USA) were performed ($n > 5$) to measure the elastic modulus as a function of the filler content (Figure S3).

■ Preparation of tooth samples for nanoindentation tests

Five freshly caries-free extracted human molars were collected after obtaining the informed consents of donors. Approval to testing these samples was granted by the Ethics Committee for Human Studies of the School & Hospital of Stomatology, Wuhan University, China. The intact teeth were sectioned along the buccal-to-lingual plane using a water-cooled precision saw (Isomet 1000, Buehler Ltd., Lake Bluff, IL, USA) and three sections from the mid-portion of each tooth were selected for tests. The produced tooth slabs (total 15 slabs) were wet-ground with silicon carbide (SiC) paper of 600 grit. The final polishing of the slab specimens were carried out in a polisher (Ecomet 250, Buehler) using diamond suspensions (particle size of 9, 3, 1, 0.25, 0.05, 0.02 μm in sequence) after embedding the slabs into epoxy blocks. The sample surface was cleaned ultrasonically and examined using an optical microscope (BX51M, Olympus, Japan) after each polishing step. The preparation steps mentioned above were carefully conducted to avoid as much as possible the generations of microcracks within the DEJ areas (Figure S5). All samples were stored at 4 $^{\circ}\text{C}$ and fully hydrated in Hanks' balanced salt solution (HBSS) with the addition of 0.05 wt.% thymol crystals to prevent demineralization and bacterial growth prior to testing; samples were additionally kept moist during testing by frequently spraying with HBSS. Three representative regions shown in Figure S5, *i.e.* lingual cusp (LC), central fossa (CF), and buccal cusp (BC) were chosen as the testing areas for the following experiments.

■ Nanoindentation tests on tooth

All the nanoindentation tests in this study were performed in the Hysitron TI 950 TriboIndenter system equipped with the latest version of the nano-dynamic mechanical

analysis package (nanoDMA III). A standard Berkovich tip with tip radius of 50 nm (Hysitron Inc.) was used for the tests. In order to achieve the highest spatial resolution for the static indentations, the minimum depth necessary for meaningful indentation and the associated minimum inter-indent spacing to prevent interference between adjacent indentations should be defined. The former was determined to be ~ 80 nm by performing continuous dynamic indentations on both the enamel and dentin, as well as the DEJ regions (Figure S6). Each dynamic test was performed at a constant strain rate of 0.05 s^{-1} with a hold time of 5 s at maximum load of 3000 μN . The frequency of the dynamic load was set to be 200 Hz, which was based on a set of preliminary tests showing that frequency had no effect on the measured dynamic modulus (Figure S7, indicating negligible viscoelastic effects). The minimum inter-indent spacing was then determined by conducting series of displacement-controlled quasi-static indentations (80 nm maximum depth) on both the enamel and dentin with intervals varying from 1 μm to 10 μm . Results (Figure S8) showed that 2 μm was the appropriate value for the minimum spacing.

Nanoindentation arrays based on the above-defined parameters were configured within a $30 \times 30 \mu\text{m}^2$ area covering both the enamel and dentin in such a manner that the long line of the array intersected obliquely with the optical DEJ (included angle of $\sim 15^\circ$, Figure S9b). This was to further improve the spatial resolution of the tests to better capture the mechanical transitions from dentin to enamel. The distance between each indent and the optical DEJ (schematically drawn in Figure S9b) was determined by processing the in-situ post-images (insets in Figure S9c-S9e) to find the shortest distance using computer codes written in Matlab. At least 3 arrays were repeated for one location in a specimen and data from all specimens were plotted together as shown in Figure S9c-S9e.

Modulus mapping tests were also performed within the DEJ regions to obtain spatially continuous distributions of the dynamic modulus. Such a test was accomplished by superimposing a small sinusoidal (AC) force on top of a constant quasi-static (DC) force

during the raster scanning imaging process [s5]. Dynamic modulus as a function of spatial position could be extracted according to the recorded displacement responses as detailed in the literature. In this study, raster scanning was performed at a scan rate of 0.1 Hz over a $10 \times 10 \mu\text{m}^2$ region covering both the enamel and dentin. The static force for imaging was set to 2 μN throughout and the dynamic force applied at a frequency of 200 Hz was set to 2 μN for enamel and 1 μN for dentin to achieve similar displacement amplitudes for both regions. By superimposing and analyzing data from two scans of the exactly same region using different dynamic forces, a 3D map containing both information of the dynamic modulus and surface topography was collected at a 256×256 pixel resolution (Figure S9a).

- Fabrication and characterizations of the resin-composite bilayers (RCBs) with sharp, step, and bio-inspired functional gradient interfaces (FGI)

The fabrication process of the RCB with FGI was schematically shown in Figure 2a. Briefly, uncured pure resin (Bis-GMA/TEGDMA) and highly-filled composites (36 vol.%) poured in a glass dish (25 mm in diameter and 1 mm in specimen thickness) were first pre-polymerized to reach their respective gelation point ($\sim 10\text{-}20\%$ double bond conversion) [s4, s6]. This was realized by applying an ultra-low light irradiation ($50 \text{ mW}/\text{cm}^2$ for 10 s) onto the specimens (steps 1 and 2). The pre-polymerization was to pre-solidify the resins and immobilize the nanofillers inside the composite layer while still allow covalent bonds to be formed at the surfaces of both layers during later curing process. Subsequently, interphase layer with thickness of $\sim 10 \mu\text{m}$ composed of composite with intermediate filler content (18 vol.%) was spin-coated onto the resin gel (step 3). The composite gel (36 vol.%) was then transferred onto the uncured interphase layer to form a pre-shaped sandwiched structure (step 4). The resin-interphase-composite multilayer was further clamped onto a vibrating stage (AS 200 basic, Retsch, Germany) running at a vibration amplitude of $\sim 0.1 \text{ mm}$ along the specimen thickness direction and a frequency of 20 Hz while exposed to a static magnetic

field to migrate the nanofillers within the interphase layer (step 5). The magnetic field was generated by a permanent magnet mounted right on top of the specimen with the intensity adjusted by the space between them. An optimized magnetic field intensity of 150 mT (measured with a 410 Handheld Gaussmeter, Lakeshore, corresponding to a magnet-specimen space of ~ 2 mm) and exposure duration of 20 min were determined to form a continuously gradient filler distribution based on our theoretical predictions (Supplementary Text 1) validated by experiments (Figure 1). The redistributed multilayer was then transferred into a vacuum chamber for 1 h to degas bubbles and to stabilize the mixture. The RCB with FGI was finally polymerized by applying a full light irradiation of 1000 mW/cm² for 40 s (step 6).

As the control, RCBs with sharp and step interfaces were also fabricated. The sharp interface was obtained by directly polymerizing the resin gel and the composite gel together without including the interphase layer. The step interface was fabricated using a similar procedure as the FGI except that the magnetic exposure step (step 5) was excluded.

The completely cured RCBs with various interfaces were characterized by optical microscope, TEM, and TriboIndenter. Samples were first sectioned along a plane perpendicular to the interface and mirror-polished to obtain a smooth cross-sectional surface. Optical microscope (BX51M) was used to determine the interfacial integrity and thickness. The spatial distributions of the nanofillers within the interfacial regions were examined by TEM (JEM-2100). Displacement-controlled nanoindentation tests (maximum depth of 200 nm, inter-indent spacing of 2 μ m, 100-nm Berkovich tip) were performed along the interphases to measure the spatial variations of the mechanical properties. The indent arrays were configured crossing the interphase from resin to composite with a small included angle of $\sim 20^\circ$ between the array line and the interface line to improve the spatial resolution of the tests (Figure 2d). Repeated tests ($n = 5$) were carried out to obtain standard deviations of each position within the interfacial regions.

■ Mechanical tests of RCBs with various interfaces

Hertzian contact tests ($n = 3$) were performed to evaluate the contact resistance of the RCBs with different interfaces. The tests were carried out in an Instron 5500R universal testing machine (Instron Corp., Canton, MA, USA) with a 20-mm-diameter hemispherical tungsten carbide probe loading from the composite side of the RCBs. A loading rate of 5 N/s was selected for the contact tests. By simultaneously recording the load and displacement data, critical load defined as the load of the first point of displacement jump (Figure S10) was determined and compared for the different interfaces. This point has been reported to correspond to the pop-in of radial cracks in the top composite layer. Preliminary tests showed that varying the loading rate resulted in varying critical loads but did not alter the relative ranking of the interfaces tested in terms of the critical load.

Three-point bending tests ($n = 3$) were also performed to assess the crack propagation and interfacial fracture behaviors of the RCBs with different interfaces. The fabricated 25-mm-diameter disc-shaped samples were cut into bars measuring $15 \times 2 \times 2 \text{ mm}^3$ and ground with 600, 1200, and 2400 grit SiC papers. Flexural tests were carried out in the Instron 5500R system equipped with a three-point bending rig. Bending was applied from both sides of the RCBs (*i.e.* composite side loaded in tension and resin side loaded in tension) using a low displacement loading rate of 0.05 mm/min with a span of 10 mm. Samples were loaded until fracture occurred and force-displacement data were monitored continuously and converted to effective stress-strain curves according to sample dimensions. Crack profiles of the fractured samples were observed and captured using an optical microscope (Axio Scope A1, Zeiss, Germany). During the tests, loading process was stopped at certain points also for crack profile documentation (Figure S11 and S12). For comparison, samples made of pure resin and pure composite (36 vol.%) were also tested following the same procedures described above.

■ Durability tests of RCBs with various interfaces

A home-built setup composed of a controllable temperature mount (model 226,

Arroyo Instruments) and an acoustic emission (AE) device (PCI-2, Physical Acoustic Corporation, Princeton Junction, NJ, USA) was assembled to test the durability of the RCBs with different interfaces (Figure S13a). The temperature mount was controlled by a LabView program through the 6340 ComboSource controller. The thermal plate of the mount was programmed to output a cyclic sinusoidal temperature wave ranging from 5 °C to 90 °C with one cycle duration of 70 s (Figure S13b). For a durability test, RCB sample was placed onto the thermal plate with the resin side facing downward. The actual temperature of the top composite surface was measured by a T-type miniature thermocouple (Omega Engineering Inc., Stamford, CT, USA) and showed a similar sinusoidal pattern ranging from ~15 °C to ~80 °C (Figure S13b). An AE sensor (Nano30, Physical Acoustics) was attached to the composite surface with grease to monitor any AE signal caused by interfacial cracking and/or debonding during the cyclic thermal loading. The signal was collected at 2 MHz sampling rate, 2 ms duration and 70 mV threshold. The cyclic thermal loading and AE signal monitoring were performed continuously for 48 h or until obvious interfacial debonding (based on the AE signal and visual observation) occurred, whichever came first. For each RCBs, at least 3 replicates were conducted. AE parameters such as event number, event time and signal amplitude were analyzed and compared between the different RCBs. After each test, the cross-section (side view) of the sample was observed and captured by an optical microscope as shown in Figure S14 (BX51M, Olympus).

■ Fabrications and tests of nanocomposite coatings with different filler distributions

The FGC was fabricated using similar steps as shown in Figure 2a except that the top composite layer was not included (*i.e.* steps 2 and 4 in Figure 2a were excluded). By magnetically redistributing the nanofillers inside the nanocomposite coating (thickness of ~10 µm, filler content of 18 vol.%), a FGC with the nanofillers gradiently distributed towards the top surface was obtained on pure resin substrate. As the control, coatings made of uniform

nanocomposites (filler content of 18 vol.% and 36 vol.%, respectively) were also fabricated by directly spin-coating and polymerizing the respective uncured composite on the resin substrate, *i.e.* without using magnetic field to control the filler distributions. The 18 vol.% and 36 vol.% composite coatings are respectively denoted as lower-filled coating (L-C) and higher-filled coating (H-C) in this study.

Nanoindentation and multiple nano-scratch patterning (nano-wear) tests were performed to respectively characterize the surface mechanical properties and wear-resistance of the prepared resin substrate, L-C, H-C, and FGC. The nanoindentation tests were conducted at randomly-selected spots ($n > 5$, at least 100 μm apart) of each sample using a 100-nm Berkovich tip run in load-control mode with the maximum load of 8000 μN . The nano-wear tests and in-situ pre/post scanning imaging were carried out using a conical-shaped tip with the tip radius of 0.5 μm and cone angle of 60° (Hysitron Inc.). The specific steps for the wear test were detailed in our previous study [s7]. Briefly, after pre-scanning a $10 \times 10 \mu\text{m}^2$ square area under a small load of 1 μN , the indenter tip was driven along the longitudinal direction for a round trip under a constant wear load at a velocity of 0.8 $\mu\text{m/s}$, the tip was then moved laterally by ~ 7 nm for next longitudinal scratch. This longitudinal scratch and lateral movement were repeated until the scratches covered the whole testing region ($2 \times 2 \mu\text{m}^2$ inside the pre-scanning area), which was counted as one pass wear. The $10 \times 10 \mu\text{m}^2$ area covering the worn region was scanned again after the test. Wear volume was calculated based on computer programs utilizing the pre/post-scan images as described in our previous study [s7]. In this study, wear load and wear pass were selected as 80 μN and 10, respectively. Preliminary tests showed that varying these parameters did not alter the relative ranking of the different coatings tested based on the wear volume. For each sample, the wear test was repeated for at least 3 times.

Durability tests of the different coatings were conducted using the same setup as shown in Figure S13a. To better observe and capture the regional ruptures of the coating/resin

interface, the samples were cut into cubes of approximate dimensions of $10 \times 10 \times 1 \text{ mm}^3$. Cyclic thermal loading as shown in Figure S13b was applied to the L-C, H-C, and FGC samples for 24 h or until apparent interfacial cracking/debonding or coating rupture occurred, whichever came first. The cross-section surface of each sample was observed and captured by an optical microscopy (BX51M, Olympus) after every 100 cycles of the thermal loading.

The periodic multilayer coating (PMC- n) was fabricated by repeatedly depositing the FGC gel on top layer by layer until the desired layer number n was reached. During each deposition, the filler loading of the nanocomposite, the thickness of the composite layer, and the intensity and direction of the magnetic field for nanoparticles redistribution were precisely controlled to modulate the architectures of the resulting PMC. For the PMC-9 demonstrated in Figure 3d-3g, composites with 10, 13, 16, and 18 vol.% $\text{Fe}_3\text{O}_4@\text{SiO}_2$ with respective layer thickness of 25, 20, 15, and 10 μm were adopted in sequence from the innermost to the outermost FGC. During each layer deposition, the direction of magnetic field was altered by changing the position of the permanent magnet relative to the specimen (*i.e.* switching between ‘right on top’ and ‘right below’). The PMC- n with oscillating mechanical properties and a periodic pitch of the thickness of 2 FGC layers was obtained by curing the multiple FGC gels together. Nanoindentation tests ($n = 3$) and TEM characterizations were performed using similar procedures described above for the RCB with FGI.

- Fabrications, characterizations, and tests of biomimetic adhesives with compliant-, stiff-, and functional gradient pillars (CPs, SPs, and FGPs)

The FGPs were fabricated by a well-established mould replication method combined with our magnetic-field migration technique as shown schematically in Figure 4a. Silicon masters (area of $2 \text{ cm} \times 2 \text{ cm}$) with patterned holes of 2.5 μm diameter, 10 – 30 μm length with a step of 10 μm (corresponding to aspect ratios (ARs) of 4, 8, and 12), and 6 μm center-to-center distance were prepared by photolithography followed by deep reactive-ion etching

(step 1). The UV-curable PUA resins (measured density of 1.02 g/cm^3 and viscosity of $\sim 0.16 \text{ Pa}\cdot\text{s}$ at room temperature) mixed with 15 vol.% (29.5 wt.%) silanized $\text{Fe}_3\text{O}_4@\text{SiO}_2$ nanoparticles were drop-dispensed onto the master and covered with a thin polyethylene terephthalate (PET) film acting as the backing layer (step 2). The viscous composite were filled into the high AR holes by a vacuum-assisted capillary filling process. The master, the backing layer, and the infiltrated resin composite were then transferred onto the vibrating stage and exposed to a static magnetic field (150 mT for 30 min) facing the backing layer side to migrate the nanofillers inside the infiltrated composite (step 3). After degassing and stabilizing in a vacuum chamber for 1 h, the patterned and redistributed resin composites were cured by applying a UV irradiation of 500 mW/cm^2 for 2 min (LZ1-10UA00, LED Engin Inc.) (step 4). The solidified PUA replica backed with the PET film was subsequently peeled off from the silicon master (step 5), and further cured with additional UV irradiation for 5 min to completely crosslink the polymer of the composite pillars (step 6).

As the control, unpatterned PUA film (*i.e.* flat PUA), compliant pillars (CPs) made of pure PUA, and stiff pillars (SPs) made of homogeneous PUA/ $\text{Fe}_3\text{O}_4@\text{SiO}_2$ nanocomposites (15 vol.%) were also fabricated. The CPs and SPs were fabricated by pouring the respective material (*i.e.* pure PUA and 15 vol.% PUA/ $\text{Fe}_3\text{O}_4@\text{SiO}_2$ nanocomposites) onto the silicon master and directly curing them without applying magnetic exposure.

The fabricated micro-pillar structures (CPs, SPs, and FGPs with different ARs) were sputter-coated with a 5-nm-thick Pt film and visualized *via* a field-emission scanning electron microscopy (FE-SEM, Sirion 200, FEI). The cross-sectional views were obtained by cryogenic fracture of the sample in liquid nitrogen. Transmitted optical micrographs of the pillars were also captured using the Zeiss Axio Scope A1 optical microscopy to reveal the structural differences between the CPs, SPs, and FGPs.

The spatial variations of the local stiffness (*i.e.* elastic modulus) along individual micropillars were evaluated by static nanoindentation tests. The micropillars for testing were

scraped from the backing layer and transferred onto a thin, uncured dental resin layer (Bis-GMA/TEGDMA of 70/30 by weight, thickness of a few microns) pre-spread on a glass slide. After stabilizing the mixture for a few minutes, the resin layer was cured by a blue light irradiation to provide support and clamp for the pillars. Displacement-controlled nanoindentation tests (maximum depth of 200 nm, 100-nm Berkovich tip) were performed on the exposed pillars from tip to base with the inter-indent spacing of 2 μm . For each type and each AR of the pillars, at least three replicates were tested. After the tests, the surfaces of the pillars partly embedded in the resin support were scanned by an atomic force microscopy (AFM, DI Innova, Bruker) to obtain the morphology of the residual indent pits on the pillars.

Repeated shear adhesion tests were performed using a home-built hanging setup as detailed in our previous study (see schematic diagram in Figure S18a) ^[s8]. Briefly, the testing sample was first glued to a glass slide from the backing layer side, while the pillar side of the sample was then brought into contact with a fixed glass slide (representing smooth surface) or Si wafer (representing rough surface, see Figure S18 for the surface morphologies and profiles scanned by AFM) under a preload of 1 N/cm². A weightless wire, supported by a pulley in the middle, was used to connect the glued sample/glass with a hanging weight. The height of the pulley was adjusted to ensure a pure shear force exerted to the sample. The test was started with a small weight of 20 g to keep the system steady. Smooth increment was successively added until detachment occurred. For each sample, 200 repeated trials were performed to test the durability of the shear adhesion. After the repeated tests, morphologies of the micro-pillars were observed again using the FE-SEM.

■ Finite element analysis (FEA)

Finite element simulations were performed (Abaqus/Standard v. 6.13) to show and compare the stress/strain fields of the RCBs with different interfaces during the Hertzian contact, 3-point bending, and cyclic thermal loadings. For the Hertzian contact and thermal

loading conditions, 2D axisymmetric models composed of CAX4R elements were adopted; while for the 3-point bending loading, a 2D plane-strain model with CPE4R elements (4-node bilinear plane strain quadrilateral) was built. To model the gradient in the RCBs with FGI, the interphase layer was divided further into 20 isotropic sublayers. The elastic modulus, coefficient of thermal expansion (CTE), and Poisson's ratio of each sublayer were obtained through sigmoidal interpolation (based on Figure 2g) from the values of pure resin and composite with 36 vol.% filler content. Linear rule of mixtures was used to estimate the CTE and Poisson's ratios of the composite based on the respective values of the matrix and the filler ($115 \times 10^{-6} / ^\circ\text{C}$ and $0.55 \times 10^{-6} / ^\circ\text{C}$ for the CTE, 0.35 and 0.17 for the Poisson's ratio, respectively). Perfect bonding was assumed for the interfaces between each pair of adjacent layers/sublayers and frictionless contact was also assumed. The loading and boundary conditions were kept the same as those applied in the experiments.

For the FEA of the micropillar deformations during the shear adhesion tests, only pillars with diameter of 2.5 μm and height of 10 μm (*i.e.* AR = 4) were modelled. For other ARs, similar simulation results could be obtained. For the compliant- and stiff pillar (CP and SP), a uniform 3D stress model with C3D8R elements (8-node linear brick) was used; while for the functional gradient pillar (FGP), the model was divided into 20 isotropic disks (C3D8R elements, perfect bonding between adjacent disks assumed). Elastic constants obtained from experiments were input into the respective model to endow the pillars with three different stiffness distributions (*i.e.* CP, SP, and FGP). Poisson's ratio was taken as 0.48 and 0.40 for the pure PUA and 15 vol.% PUA/Fe₃O₄@SiO₂ composite, respectively. In order to directly compare the pillar deflections and stress/strain distributions during the shear loading, encastre boundary conditions were applied to the pillar base while a shear displacement loading of 3 μm was applied to the pillar tip for all the three types of pillar.

Supplementary Figures

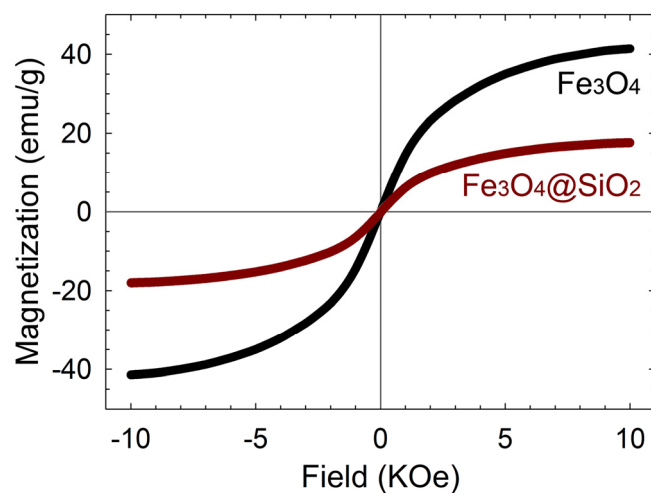


Figure S1. Field-dependent magnetization of bare Fe₃O₄ and silica-coated Fe₃O₄@SiO₂ nanoparticles at ambient temperature showing both superparamagnetic characteristics and effective screening of magnetization by silica coating (saturation magnetizations of ~40 emu/g and ~18 emu/g for respectively the bare and core-shell magnetic nanoparticles).

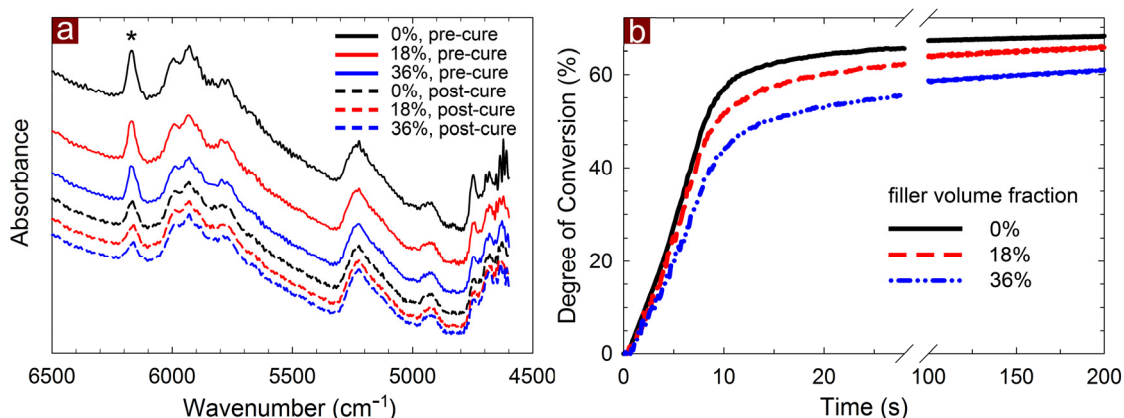


Figure S2. Polymerization kinetics of $\text{Fe}_3\text{O}_4@\text{SiO}_2$ reinforced Bis-GMA/TEGDMA nanocomposites with selected filler content measured by remote near infrared (NIR) spectrometry. a) Typical absorption spectrum of the nanocomposites before (pre-) and after (post-) photo-curing. Absorption peaks associated with the methacrylate $=\text{CH}_2$ bonds (first overtone) are highlighted by asterisk at 6165 cm^{-1} , based on which the real-time double-bond conversion shown in b) is calculated [s9]: $\text{conversion} = (1 - \text{Area}_{\text{polymer}}/\text{Area}_{\text{monomer}}) \times 100\%$, where $\text{Area}_{\text{monomer}}$ is the peak area of the sample prior to the start of irradiation and $\text{Area}_{\text{polymer}}$ is the peak area at each time point during the polymerization process. As can be seen from b), varying filler loading significantly affected the rate of polymerization with the composite with lower filler content cured faster. This trend is in line with our previous study [s10] and has been well explained by factors from material composition, light scattering, and reaction exotherm as detailed in that study and also in the literature [s11]. As also observed in b), composites with different filler content reached almost the same level of final degree of conversion as time evolved, also agreeing with our previous study [s10] and indicating negligible contribution of the chemical reaction on the mechanical properties of the nanocomposites with different filler contents studied. Therefore, the prepared resin-composite bilayers (RCBs) with various interfacial transitions can be assumed to exhibit similar and uniform distribution of the degree of polymerization throughout the sample.

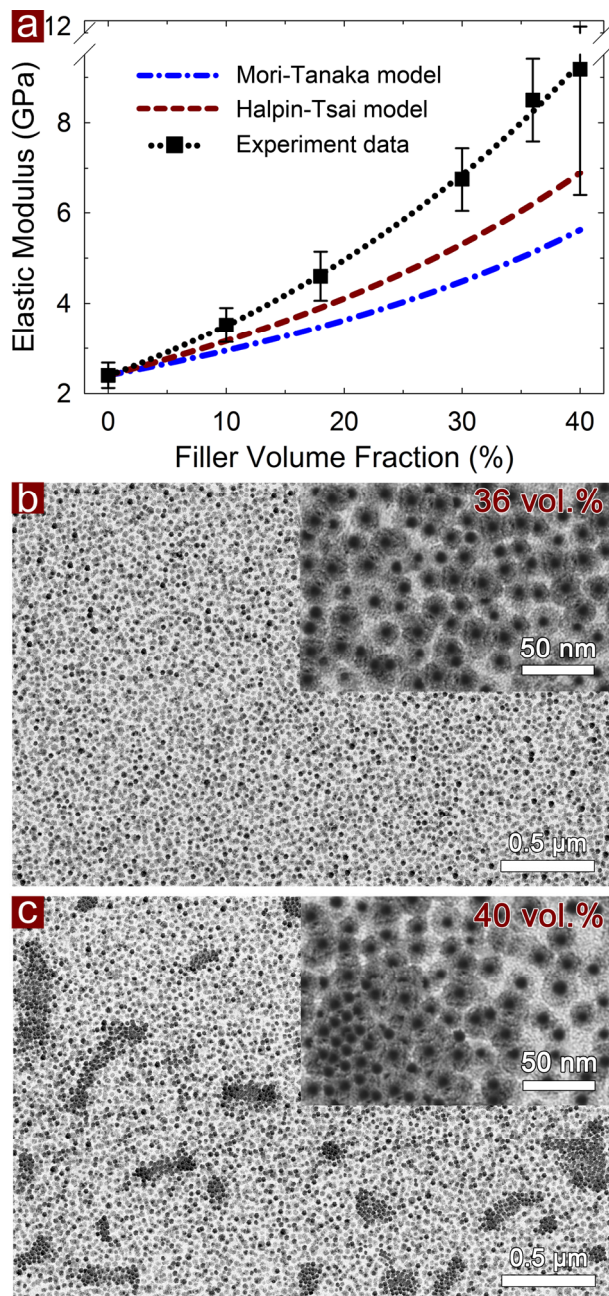


Figure S3. Effect of filler content on elastic modulus of Fe₃O₄@SiO₂ reinforced Bis-GMA/TEGDMA nanocomposites and spatial distributions of the nanofillers inside resin matrix at selected volume fractions. a) Experimental data and theoretical predictions of the elastic modulus as a function of filler content based on Mori-Tanaka and Halpin-Tsai models (Supplementary Text 2). Dotted line connecting experimental data is obtained by curve fitting using a simple exponential growth function $f(x) = a + b \exp(cx)$ where the fitting parameters a , b , and c are obtained respectively as -1.2899, 3.6796, and 0.0265 ($R^2 = 0.9975$). This function is then used to convert the measured elastic modulus back to filler volume fraction to compare the spatial distribution of the nanofillers with the computational results as shown in Figure 1b. TEM images showing contrasting dispersion states of the nanofillers when the resins are reinforced with b) 36 vol.% and c) 40 vol.% Fe₃O₄@SiO₂ nanoparticles. As can be seen, nanoparticles tended to cluster and agglomerate for the composite with 40 vol.% filler content, which corresponded to the significant standard deviation of the elastic modulus measured shown in a). For the 36 vol.% nanocomposites, a fairly uniform distribution of the fillers was observed. Therefore, 36 % was taken as the maximum volume fraction for the subject nanocomposites in this study.

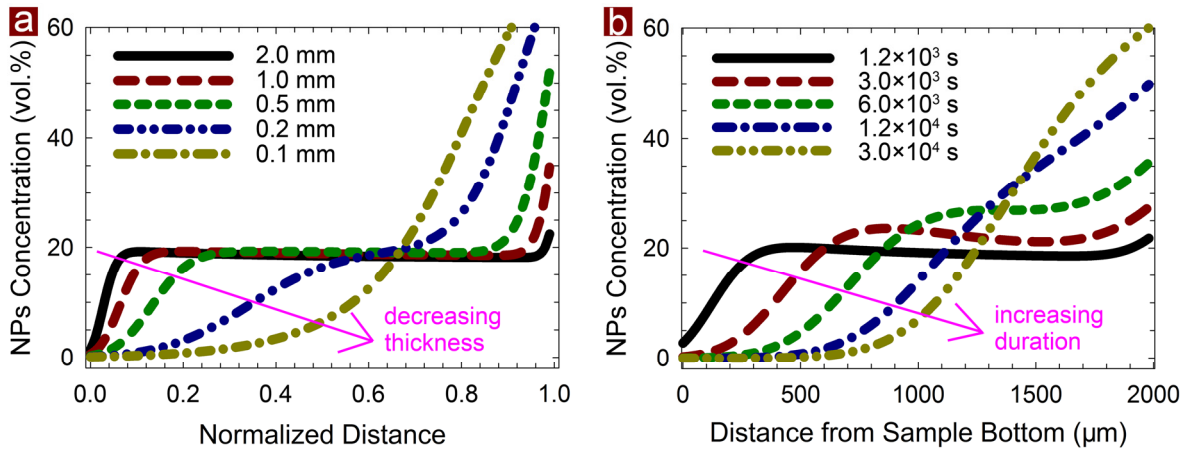


Figure S4. Theoretical calculations showing the scale-dependent processability of the magnetically-actuated functional gradient nanocomposites (FGNCs). a) Computed nanoparticle concentration along the normalized distance (*i.e.* distance from sample bottom divided by sample thickness) for sample thicknesses ranging between 0.1 and 2.0 mm at a sufficiently long processing duration of 1.2×10^4 s. Same material parameters and magnetic field conditions as those adopted in experiments (*i.e.* shown in Table S1) were used for the computations. It is seen that the concentration gradient of the nanoparticles (NPs) can be obtained for samples with thickness less than 0.2 mm ($200 \mu\text{m}$) while it is very difficult to generate such gradient if the sample is thicker than 0.5 mm ($500 \mu\text{m}$) due to weak driving force and slow particle accumulation and diffusion at distances far away from the magnetic field source (see Fig. 1a). In order to achieve gradient distribution of the NPs at large length scales, we tried modifying the material parameters in the computations to increase the driving force and accelerate the diffusion and particle accumulation processes. By changing the radius of magnetic particle to 100 nm (compared to ~ 15 nm in the experiments) and increasing the diffusion coefficient by 2000 times while keeping other parameters the same, we obtained the real-time evolution of the particle concentration for 2.0 mm ($2000 \mu\text{m}$) thick sample as shown in b). It can be seen that the concentration gradient gradually forms as the processing duration evolves and eventually reaches equilibrium at a long duration of $\sim 3.0 \times 10^4$ s. Therefore, the theoretical predictions indicate that for the material compositions adopted in this study, the FGNCs should be able to be scaled up to $\sim 200 \mu\text{m}$ using realistic magnetic field intensity and processing duration. For larger length scale such as millimeters to even centimeters, the concept of FGNCs is still valid; however, the material parameters (*e.g.* particle size, viscosity of resin matrix, *etc.*) and the processing conditions (*e.g.* magnetic field intensity, processing duration, *etc.*) need to be adjusted to achieve optimal concentration gradient. Besides, the method of layer-by-layer deposition as presented by Libanori *et al.* [S12] may be considered to be combined with our FGNCs to create large objects with continuous and significant mechanical gradient.

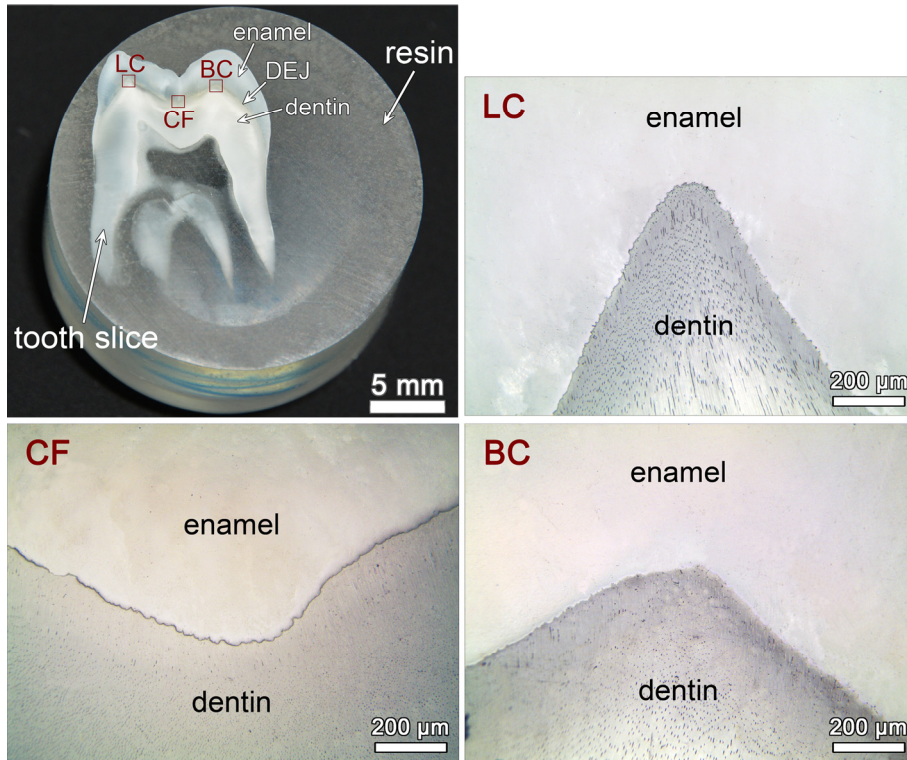


Figure S5. Photography of the prepared tooth slice sample embedded in epoxy block and typical optical microscopy images showing the details of three representative regions for testing: lingual cusp (LC), central fossa (CF), and buccal cusp (BC).

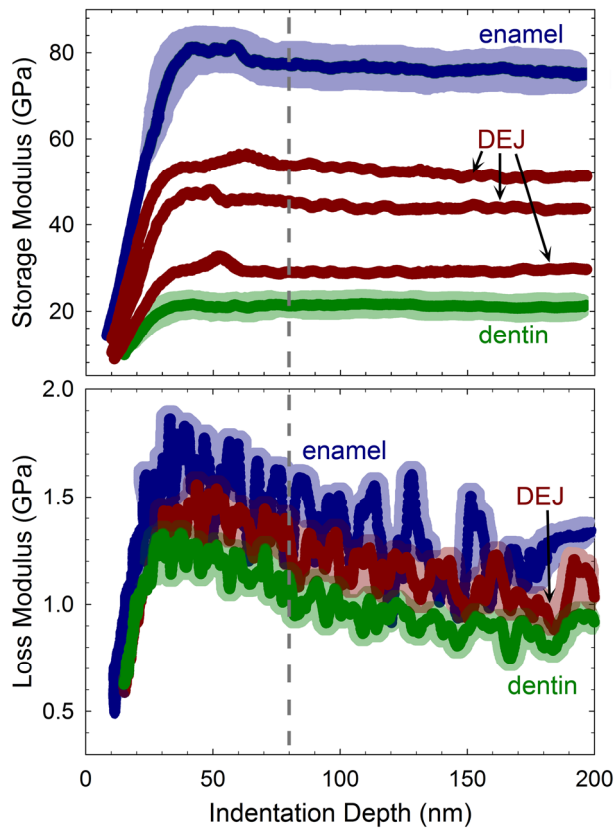


Figure S6. Dynamic modulus (storage and loss) of the tooth enamel, dentin, and DEJ regions as a function of indentation depth measured by continuous dynamic indentations using nanoDMA. Based on these data, the minimum indentation depth for static tests was determined to be 80 nm as indicated by the dashed line in the figure. Shaded areas indicate standard deviations of the tests and three random locations were tested within DEJ regions.

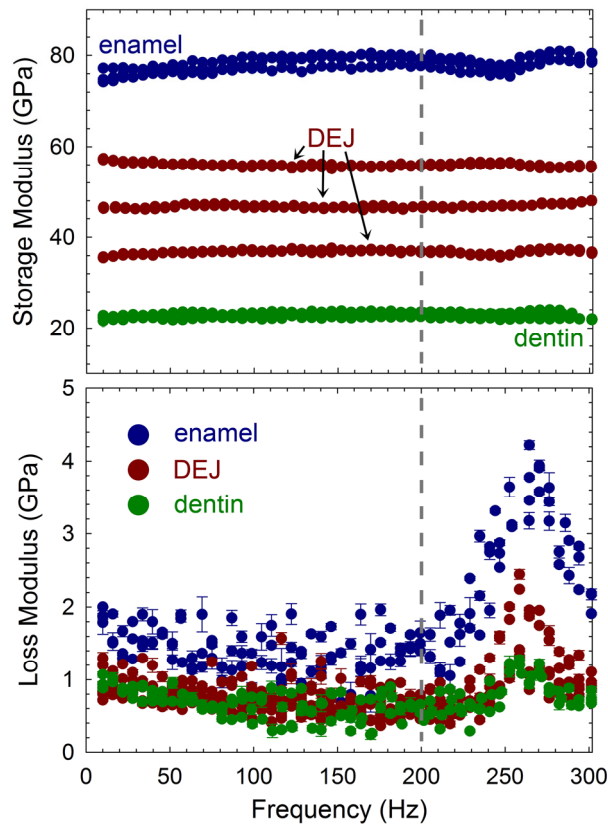


Figure S7. Frequency sweep tests ($n = 3$) showing that dynamic modulus (storage and loss) of the tooth enamel, dentin, and DEJ regions do not depend on the loading frequency, indicating minimized viscoelastic effects.

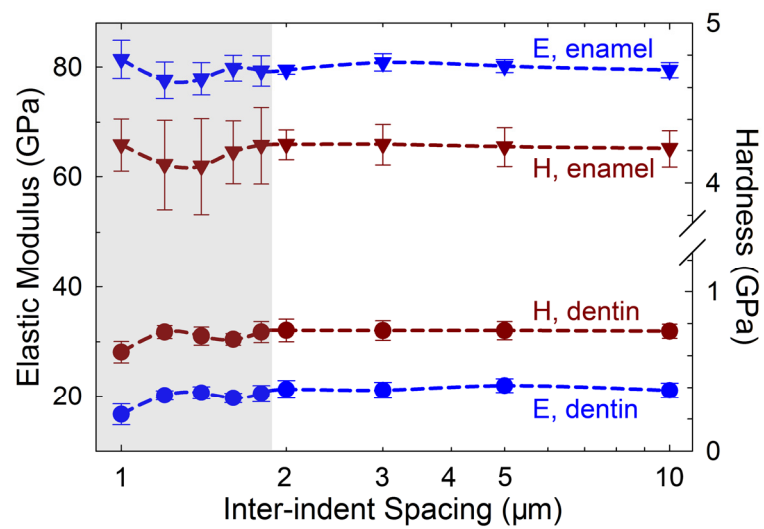


Figure S8. Elastic modulus and hardness of enamel and dentin as a function of inter-indent spacing measured by static nanoindentation tests. Shaded region indicates unstable results caused by interferences between adjacent indentations, based on which 2 μm is determined as the minimum inter-indent spacing for 80 nm indentation depth.

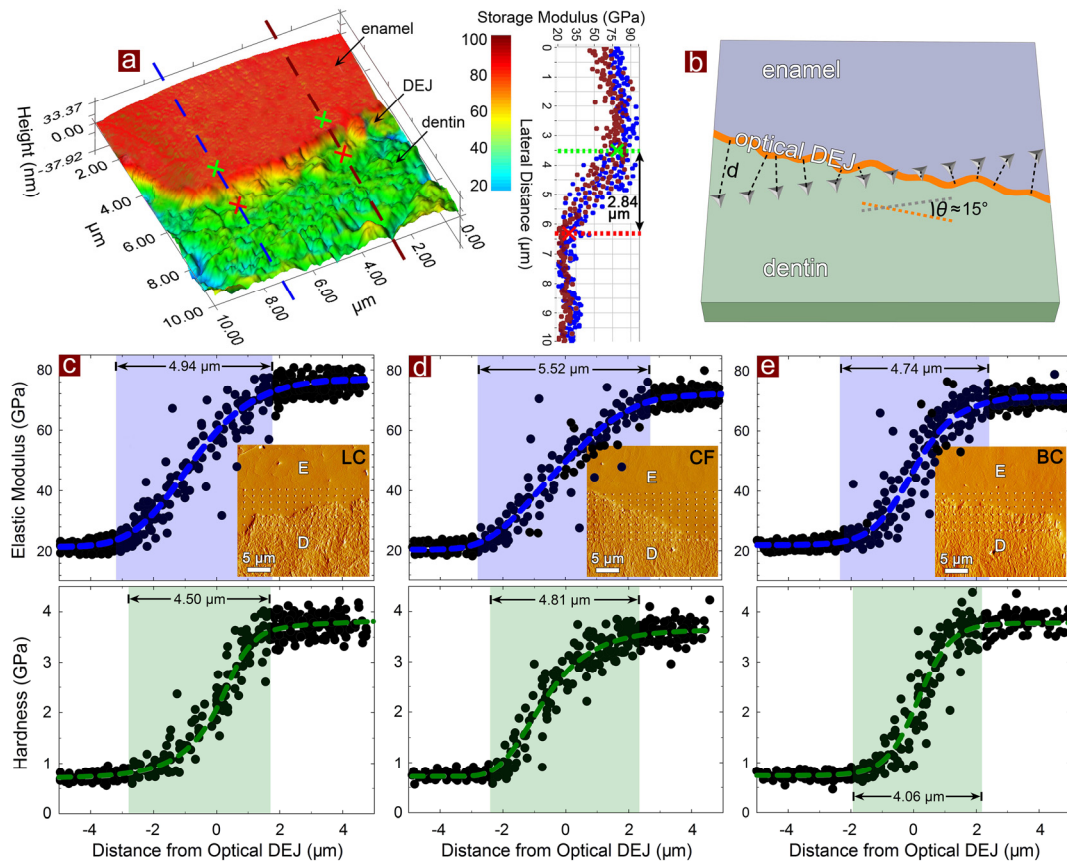


Figure S9. Results of nanoindentation tests on human teeth showing smooth mechanical gradient within the dentin-enamel junction (DEJ) region. a) Representative 3D storage modulus map of tooth DEJ obtained by dynamic modulus mapping test. Cross-sectional profiles of the modulus from two selected lines perpendicular to the optical DEJ are displayed. b) Schematic diagram showing the configuration of nanoindentation array within DEJ region to maximize the spatial resolution of the tests. Dashed segments denote the distance d between each indent and the optical DEJ. Elastic modulus and hardness determined by static nanoindentation tests as a function of the distance from optical DEJ (*i.e.*, d) are plotted in c), d), and e) for respectively the LC, CF, and BC region of tooth. Dashed lines obtained by sigmoidal fitting are provided for visual assistance. Shaded regions indicate transitional width of DEJ. Insets shows surface morphologies of the testing regions with residual indent pits obtained by *in-situ* scanning probe microscopy (SPM), where E denotes enamel and D denotes dentin. Results shown in this figure represent thus far the most detailed data for tooth DEJ, which show for the first time the sigmoidal transition (instead of linear transition widely assumed in the literature [s13, s14]) from dentin to enamel in the elastic modulus and hardness.

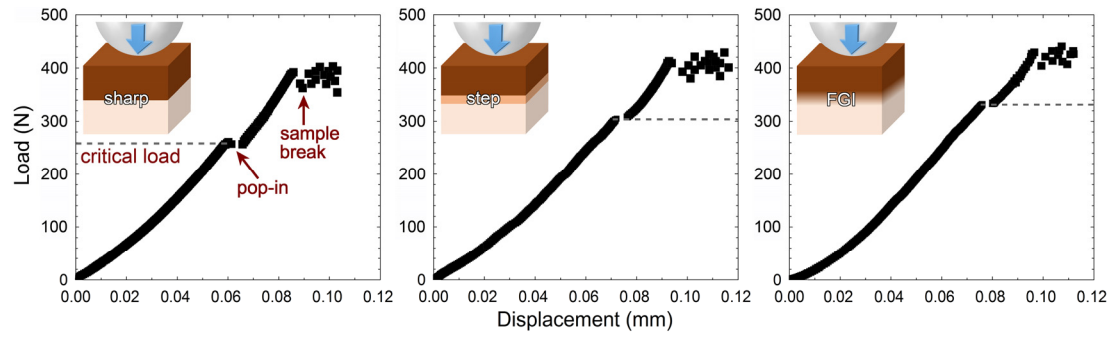


Figure S10. Typical load-displacement curve for the Hertzian contact tests on RCBs with different interfacial transition. Critical load for cracking pop-in was determined by the first point of displacement jump in the curves as indicated.

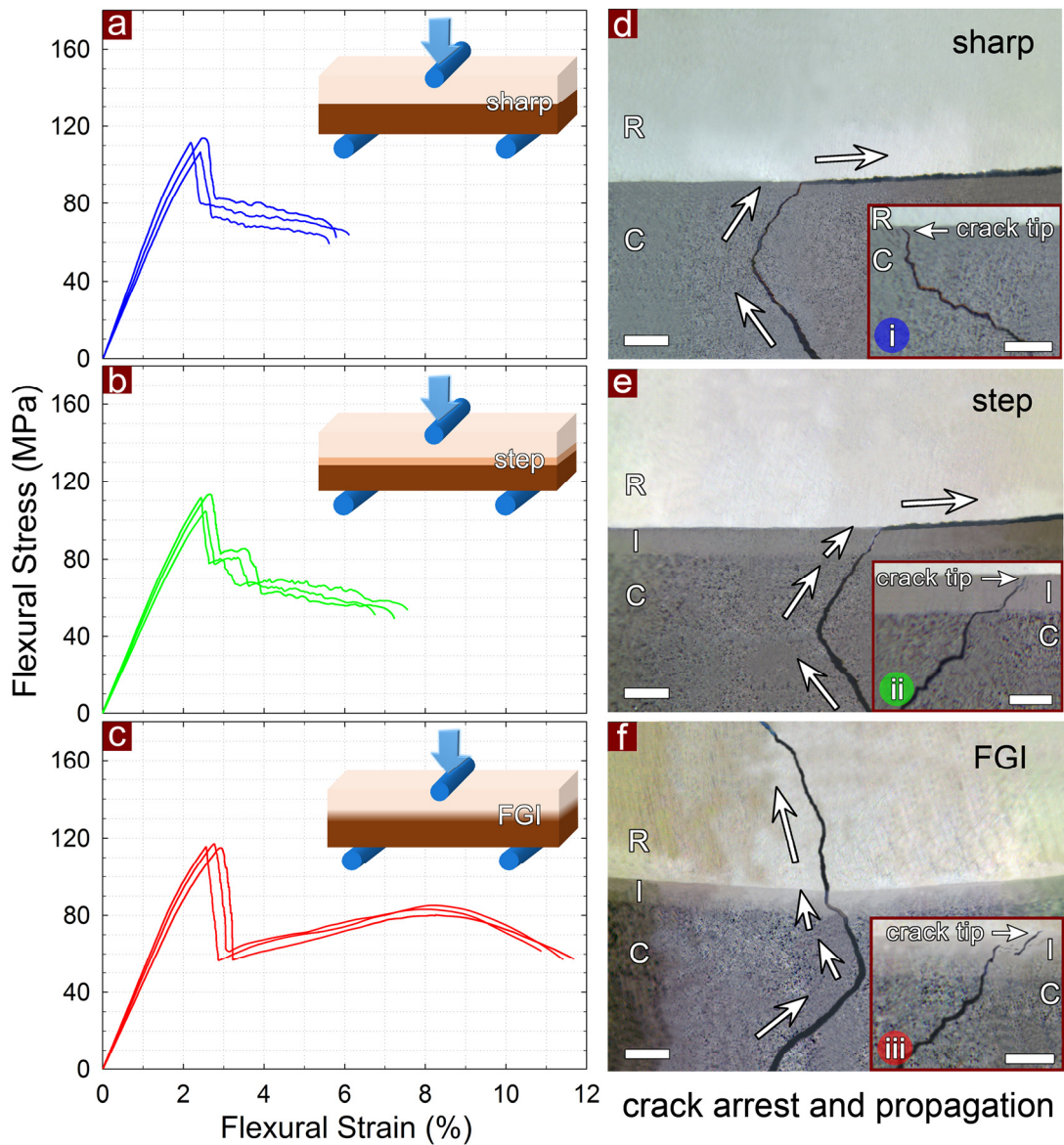


Figure S11. Effective stress-strain curves of repeated 3-point bending tests on RCBs with a) sharp, b) step, and c) FGI interfacial transition with composite side loaded in tension. Corresponding crack profiles showing the crack propagation paths near interfacial regions (indicated by solid arrows) captured by optical microscopy are displayed in d)-f). Insets in d)-f) showing crack arresting profiles during bending tests corresponding to points i-iii indicated in Figure 2i. Scale bars are respectively 20 μm and 10 μm in the images and insets.

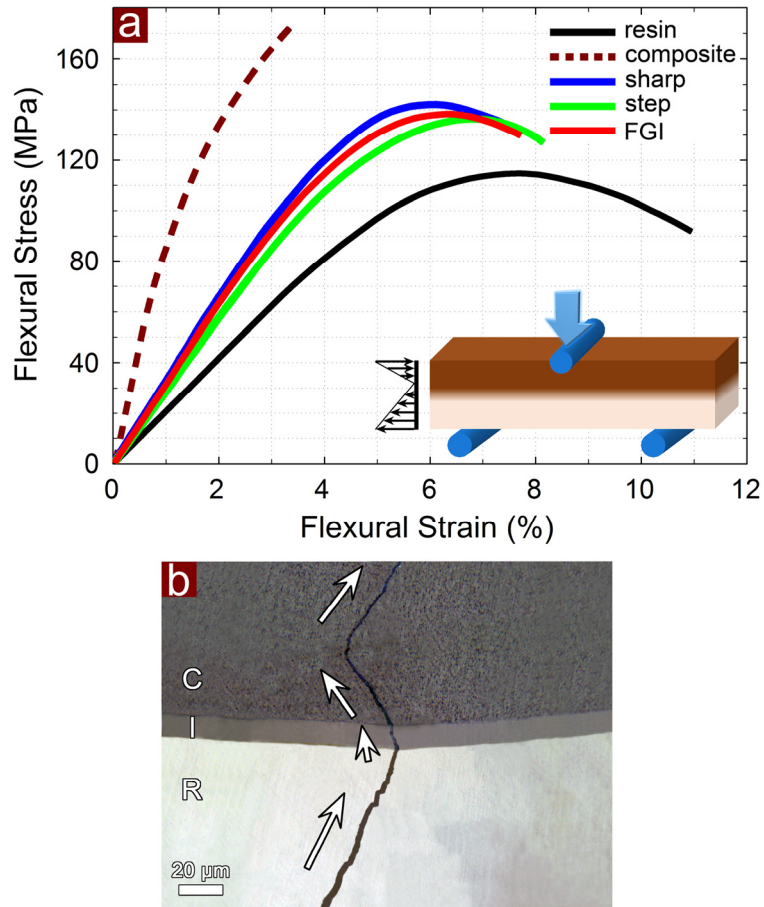


Figure S12. a) Effective stress-strain curves for 3-point bending tests on pure resin, pure composite, and RCBs with different interfacial transition with resin side loaded in tension. Normal stress distribution of the cross-section are drawn schematically by the RCB bending bar to show the shift of the neutral axis from the sample center to the composite layer. b) Crack profiles after bending tests captured by optical microscopy showing full crack propagation path near the interfacial regions as indicated by the solid arrows. Since samples fractured in a similar manner when RCBS were loaded from the resin side in tension, only the one with step transition is displayed here.

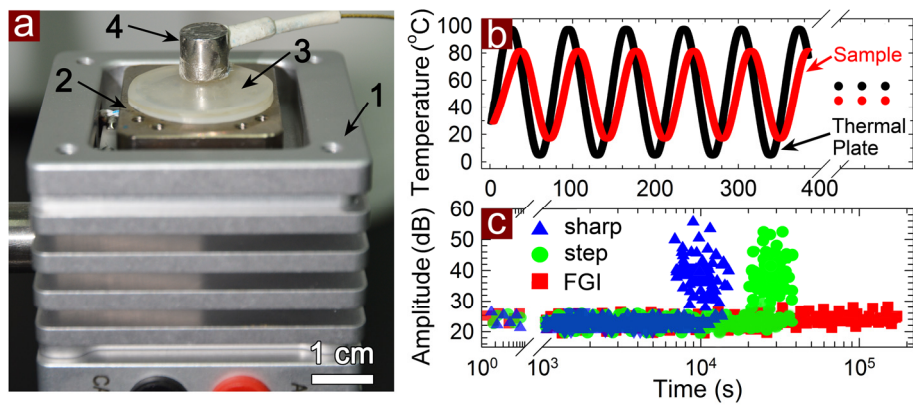


Figure S13. a) Photography of the home-built setup for interfacial durability tests: 1) mounting stage, 2) controllable thermal plate, 3) testing sample, and 4) acoustic emission (AE) sensor. b) Cyclic thermal loadings output by the thermal plate and measured at the top surface of the sample. c) Real-time AE signals monitored for RCBs with different interfacial transition during continuous 48-h tests.

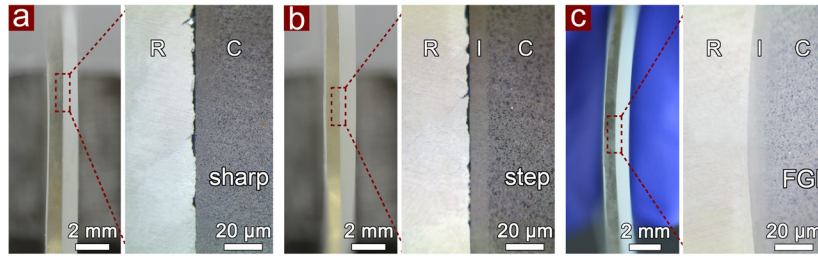


Figure S14. Photography and optical microscopy images of the samples after cyclic thermal loadings from side view showing distinct interfacial profiles for the RCBs with different interfacial transition.

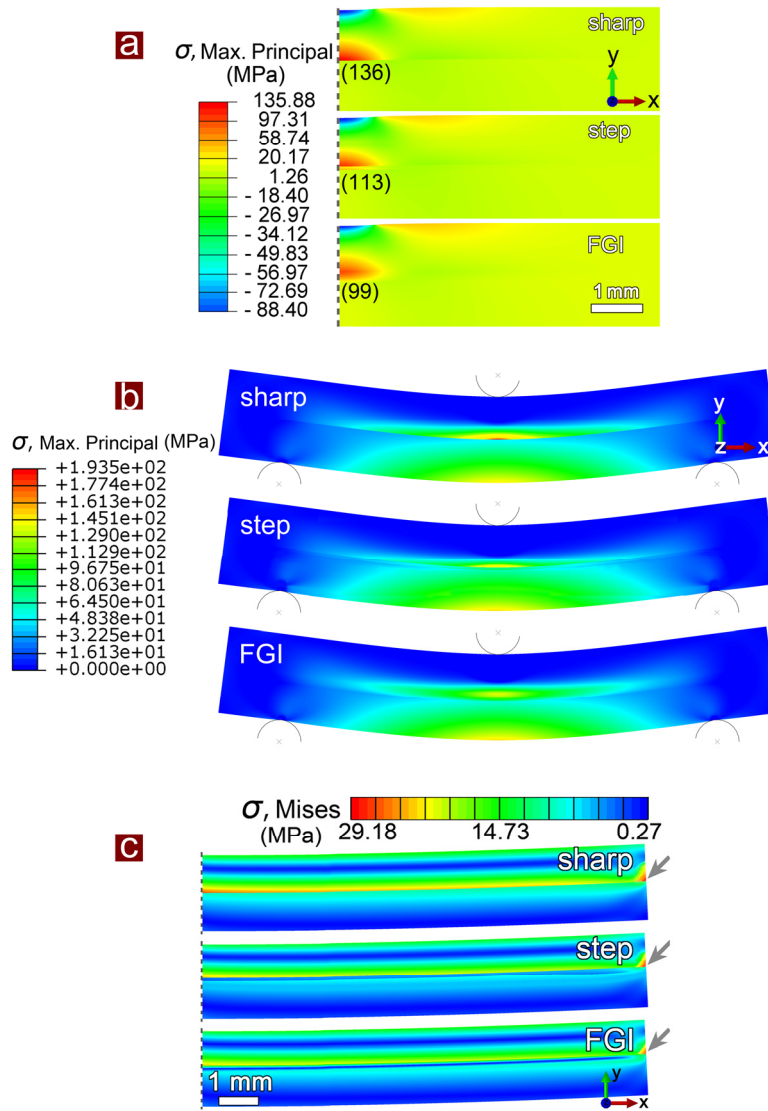


Figure S15. Stress distributions of the RCBs with different interfacial transition under experimentally-applied a) Hertzian contact, b) 3-point bending, and c) cyclic thermal loadings obtained by finite element analysis (FEA), showing mitigated stress concentrations within interfacial regions for the FGI compared with the sharp and step transition. Numbers in parenthesis in a) represent the maximum stress in each case. Gray arrows in c) indicate stress concentrations at the interfacial edge regions.

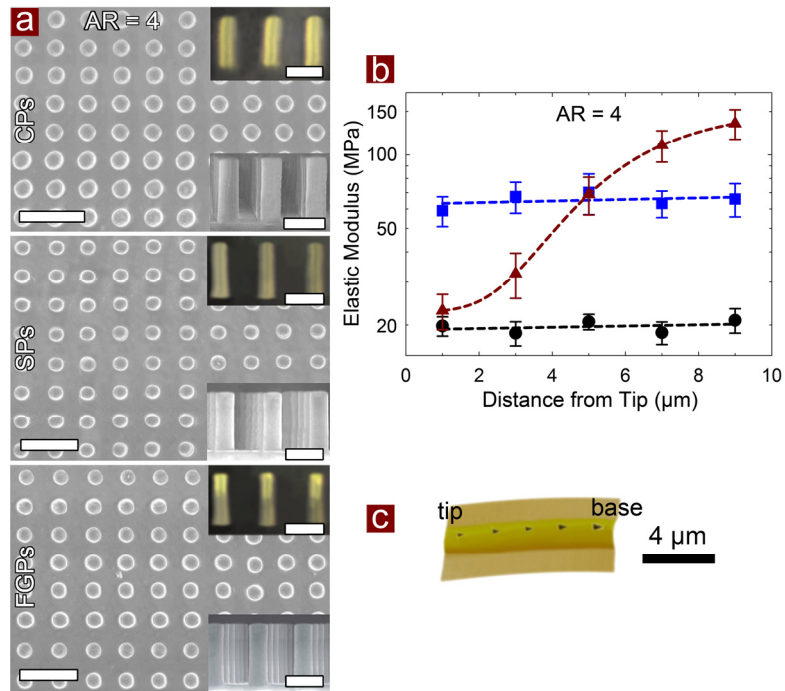


Figure S16. Characterization results of biomimetic pillars with aspect ratio (AR) of 4. a) Scanning electron microscopy (SEM) and transmissional optical images of compliant pillars (CPs), stiff pillars (SPs), and functional gradient pillars (FGPs) showing perfectly-aligned pillar structures. Scale bars are respectively 10 μm and 5 μm in the images and insets. b) Results of nanoindentation tests on individual pillars showing uniform elastic modulus for the CPs and SPs while gradually increased modulus from tips to bases for the FGPs. c) Atomic force microscopy (AFM) image of the residual indentation pits on a FGP.

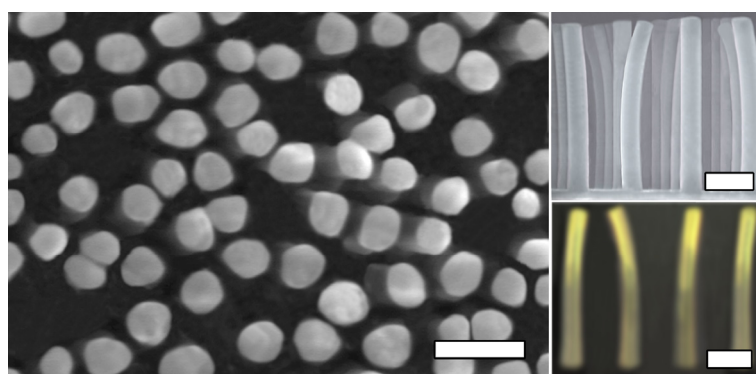


Figure S17. SEM and transmissional optical images of the fabricated FGPs with AR of 12. Scale bars are 5 μm in all images.

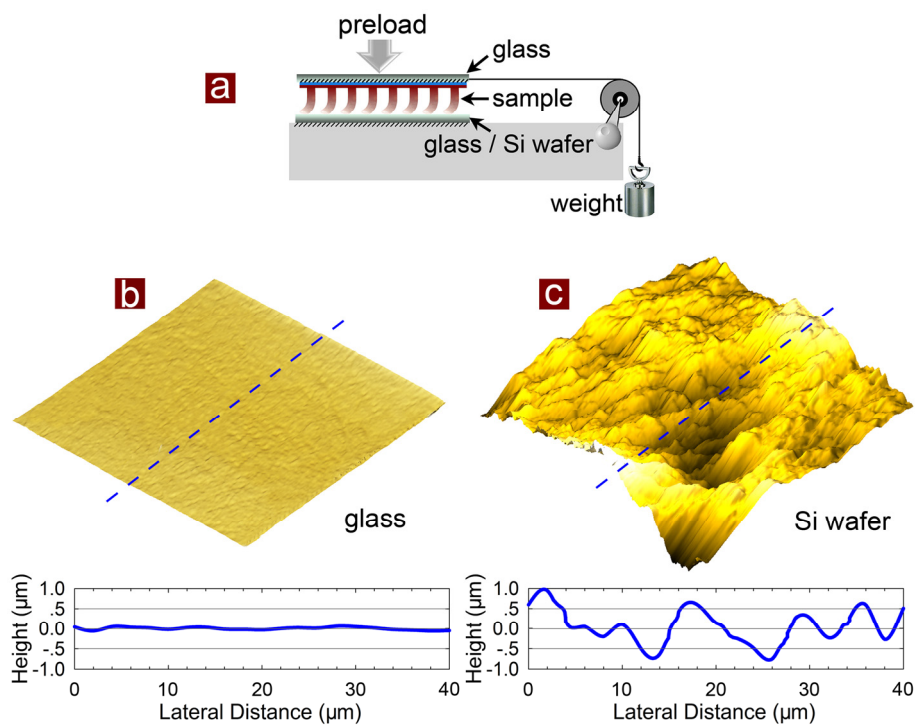


Figure S18. a) Schematic diagram of the hanging setup for shear adhesion measurement. AFM images and cross-sectional profiles of b) glass slide and c) Si wafer surface for shear adhesion tests, representing respectively smooth and coarse contacting substrate.

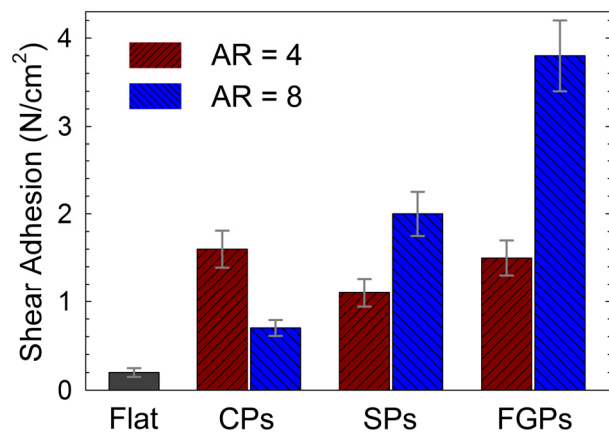


Figure S19. Shear adhesion measured for flat (*i.e.* unpatterned) PUA film and different pillar structures with AR of 4 and 8 against coarse Si wafer substrate.

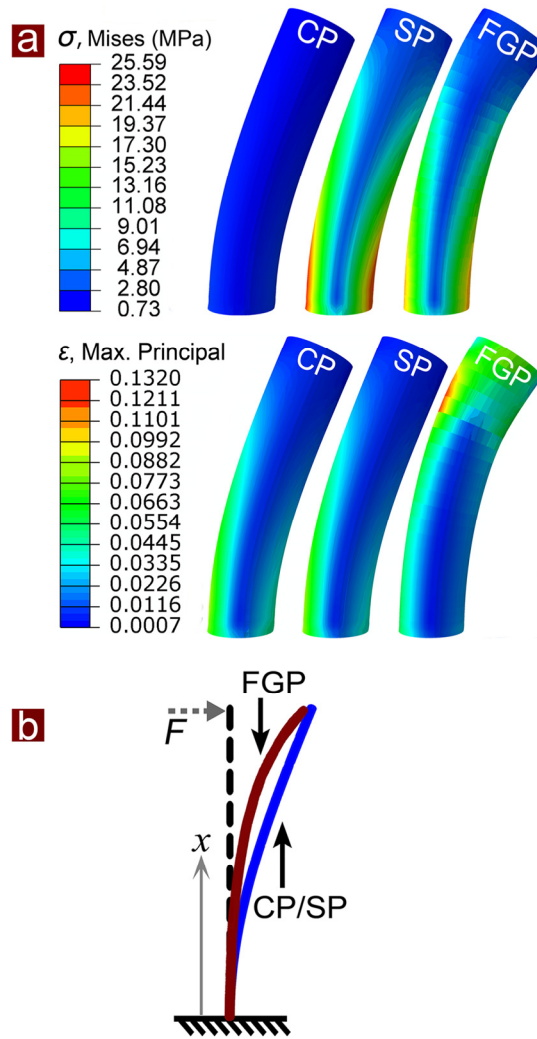


Figure S20. a) Stress and strain distributions of the different pillars under same displacement loading in the tip obtained by FEA. b) Normalized theoretical solutions to the deflection of cantilever beam made of homogeneous materials (CP/SP) and functional gradient materials (FGP).

Supplementary Texts

Text 1. Theoretical derivations and computations of magnetic field, force, and drift-diffusion transport for magnetophoresis-induced migration of nanoparticles in viscous medium.

The magnetic force is calculated by using the “effective” dipole moment method in which the nanoparticle is modeled as an “equivalent” point dipole with an effective moment $\mathbf{m}_{p,eff}$ [s15]. The magnetic force \mathbf{F}_m on the dipole is given by:

$$\mathbf{F}_m = \mu_f (\mathbf{m}_{p,eff} \cdot \nabla) \mathbf{H}_a \quad (\text{S1})$$

where μ_f is the permeability of the viscous medium and \mathbf{H}_a is the applied magnetic-field intensity at the center of the particle. The moment $\mathbf{m}_{p,eff}$ can be determined using a magnetization model developed by Furlani that takes into account self-demagnetization and magnetic saturation of the particles [s16]. The dipole moment is given by $\mathbf{m}_{p,eff} = V_p \mathbf{M}_p$ where $V_p = \frac{4}{3} \pi R_p^3$ is the volume of the particle and

$$\mathbf{M}_p = \chi_p \mathbf{H}_{in} = \chi_p (\mathbf{H}_a - \mathbf{H}_{demag}) \quad (\text{S2})$$

is the magnetization of the particle, $\chi_p = \mu_p / \mu_0 - 1$ is the susceptibility of the particle, and μ_p is its permeability. \mathbf{H}_{in} is the internal magnetic field which can be calculated by the applied magnetic field \mathbf{H}_a minus the demagnetization field \mathbf{H}_{demag} . \mathbf{H}_{demag} is the self-demagnetization field that accounts for the magnetization of the particle. Here we use $H_{demag} = M / 3$ for a uniformly magnetized spherical nanoparticle with magnetization M in free-space [s17]. Thus,

$$\mathbf{m}_{p,eff} = V_p f(H_a) \mathbf{H}_a \quad (\text{S3})$$

where $f(H_a)$ is a function of magnetic susceptibilities and can be expressed by:

$$f(H_a) = \begin{cases} \frac{3(\chi_p - \chi_f)}{(\chi_p - \chi_f) + 3}, & H_a < \left(\frac{(\chi_p - \chi_f) + 3}{3\chi_p} \right) M_{sp} \\ M_{sp} / H_a, & H_a \geq \left(\frac{(\chi_p - \chi_f) + 3}{3\chi_p} \right) M_{sp} \end{cases} \quad (S4)$$

where χ_p and χ_f are respectively the magnetic susceptibilities of the particle and fluid, and M_{sp} is the saturation magnetization of the nanoparticle. Thus, the magnetic force on the magnetic particle can be rewritten as,

$$\mathbf{F}_m = \mu_f V_p f(H_a) (\mathbf{H}_a \cdot \nabla) \mathbf{H}_a \quad (S5)$$

For simplicity, we execute 1D model along the axial (thickness) direction of the disk magnet, where the magnetic field (H_{az}) and magnetic force (F_{mz}) for a cylindrical permanent magnet can be calculated by [s17],

$$H_{az}(z) = \frac{M_s}{2} \left(\frac{z + L_m}{\sqrt{(z + L_m)^2 + R_m^2}} - \frac{z}{\sqrt{z^2 + R_m^2}} \right) \quad (S6)$$

$$F_{mz}(z) = \mu_0 V_p f(H_a) \frac{M_s^2 R_m^2}{4} \left(\frac{z + L_m}{\left[(z + L_m)^2 + R_m^2 \right]^2} + \frac{z}{(z^2 + R_m^2)^2} - \frac{(z + L_m) \left[(z + L_m)^2 + R_m^2 \right] + z(z^2 + R_m^2)}{(z^2 + R_m^2)^{3/2} \left[(z + L_m)^2 + R_m^2 \right]^{3/2}} \right) \quad (S7)$$

where M_s is the saturation magnetization of the magnet, z is the distance from the bottom surface of the magnet, and L_m and R_m are respectively the height and radius of the magnet. This 1D approximation is reasonable for this study since the diameter of the magnet is much greater than the dimensions of the specimen (*i.e.* the radial components are negligible compared with the axial ones) [s15, s18].

Due to the thickness of the specimen in this study is really small ($\sim 10 \mu\text{m}$) compared to the dimensions of the magnet and the magnet-specimen distance z_0 , the magnetic forces for

the inside nanoparticles can be assumed as constant:

$$F_{mz}(z_0) = \mu_0 V_p f(H_a) \frac{M_s^2 R_m^2}{4} \left(\frac{z_0 + L_m}{\left[(z_0 + L_m)^2 + R_m^2 \right]^2} + \frac{z_0}{(z_0^2 + R_m^2)^2} \right. \\ \left. - \frac{(z_0 + L_m) \left[(z_0 + L_m)^2 + R_m^2 \right] + z_0 (z_0^2 + R_m^2)}{(z_0^2 + R_m^2)^{3/2} \left[(z_0 + L_m)^2 + R_m^2 \right]^{3/2}} \right) \quad (\text{S8})$$

By adapting the experimental parameters listed in Table S1 into Equations S6 and S8, H_{az} and F_{mz} as a function of the magnet-specimen distance are calculated and shown in Figure 1a.

The magnetophoresis-induced particle transport can be treated as drift-diffusion process as the particles are extremely small with an average diameter of 20 nm in this study. For Fick's Second Law of diffusion, the particle volume concentration $c(t)$ can be described by ^[s15]:

$$\frac{\partial c(t)}{\partial t} + \nabla \cdot \mathbf{J} = \mathbf{S} \quad (\text{S9})$$

where \mathbf{J} is the total flux vector of the particles, t is the time, and \mathbf{S} is the source term which includes exchange occurred at material interfaces or other chemical reactions (equals to zero in this study). The total flux is the sum of the chemical term \mathbf{J}_D and drift term \mathbf{J}_F . $\mathbf{J}_D = -D\nabla c$ is due to the chemical concentration diffusion and $\mathbf{J}_F = \mathbf{v}c$ is due to the action of magnetic forces on the particles, where D is the diffusion coefficient and \mathbf{v} is the particle drift velocity. Here, $D = \mu k_B T$ is the diffusion coefficient and $\mathbf{v} = \mu \mathbf{F}_m$ is the drift velocity where $\mu = 1 / (6\pi\eta R_p)$ is the mobility of a particle with effective hydrodynamic radius of R_p in a fluid of viscosity η . The drift velocity can be calculated as $\mathbf{v} = \mathbf{v}_f + \mu(\mathbf{F}_m + \mathbf{F}_g)$, where \mathbf{v}_f is the fluid velocity, and \mathbf{F}_m and \mathbf{F}_g are respectively the magnetic and gravitational (buoyancy) force on the particles. It should be noted that the gravitational (buoyancy) force is usually negligible compared to the magnetic force for magnetic nanoparticles. Therefore, for

stationary fluid ($\mathbf{v}_f = 0$) considered in this study, the drift velocity is determined only by the magnetic force $\mathbf{v} = \mu \mathbf{F}_m$.

The conservation equation can then be rewritten to:

$$\frac{\partial c(z, t)}{\partial t} = \frac{k_B T}{(6\pi\eta R_p)} \nabla^2 c(z, t) - \frac{1}{6\pi\eta R_p} \nabla \cdot (F_{mz}(z) c(z, t)) \quad (\text{S10})$$

where z is the distance from the magnet within the specimen domain. Substituting Equation S8 to Equation S10, the drift-diffusion equation can be simplified as,

$$\frac{\partial c(z, t)}{\partial t} = \frac{k_B T}{6\pi\eta R_p} \nabla^2 c(z, t) - \frac{F_{mz}(z_0)}{6\pi\eta R_p} \nabla c(z, t) \quad (\text{S11})$$

This second order differential equation can be solved numerically using the finite-volume method (FVM) as detailed by Furlani and Ng [\[s15\]](#). Briefly, for the 1D analysis, the computational domain is discretized at an interior node as follows:

$$c_i^{n+1} = c_i^n + \frac{dt}{dz} (F_{i+1/2} - F_{i-1/2}) \quad (i = 1, 2, \dots, N_z) \quad (\text{S12})$$

where c_i^n and c_i^{n+1} represent the particle concentration at the i th computational node at time steps n and $n + 1$, dz is the length of a computational cell and $N_z dz$ is the length of the specimen with N_z the number of computational nodes. $F_{i\pm 1/2}$ is a discretized version of the flux ($D \frac{\partial c}{\partial z} - vc$) at the edges of the computational cell $z_{i\pm 1/2}$ which is computed using an upwind numerical scheme described by:

$$F_{i+1/2} = D \frac{c_{i+1}^n - c_i^n}{dz} - (\min(U_i, 0) c_i^n + \max(U_{i-1}, 0) c_{i-1}^n) \quad (\text{S13})$$

The 1D model is also extended to 2D to simulate the evolution of nanoparticle concentration under different magnetic fields as shown in Figure 1c-1e and Supplementary Movies 1 and 2 and to compare the computational results with experimental ones based on TEM observations. Some parameters used in the computations are listed in Table S1.

Table S1. Parameters used in the computations of magnetic field, force, and drift-diffusion transport.

$\eta = 0.225 \text{ Ns} / \text{m}^2$	$\rho_f = 1100 \text{ kg} / \text{m}^3$	$\rho_p = 5180 \text{ kg} / \text{m}^3$	$M_{sp} = 4.78 \times 10^5 \text{ A} / \text{m}$
$R_p = 15 \text{ nm}$	$dz = 100 \text{ nm}$	$dt = 6 \times 10^{-3} \text{ s}$	$T = 300 \text{ K}$
$M_s = 1.04 \times 10^6 \text{ A} / \text{m}$	$L_m = 5 \text{ mm}$	$R_m = 30 \text{ mm}$	$c_0 = 18 \text{ vol.}\%$

Text 2. Mori-Tanaka and Halpin-Tsai models for composite modulus prediction.

In order to predict the elastic modulus of particulate-polymer composites based on the elastic properties of the components (particle and matrix), numbers of theoretical or empirical models have been introduced in the literature (see a full description in a recent review paper [s19]). Here, two representative models (Mori-Tanaka model based on micromechanics method and semi-empirical Halpin-Tsai model based on numerical modelling) are selected and compared with our experimental results of the Fe₃O₄@SiO₂ reinforced Bis-GMA/TEGDMA nanocomposites.

Mori-Tanaka model for composite modulus prediction [s20]:

$$E_c = \frac{9\tilde{K}_c\tilde{G}_c}{3\tilde{K}_c + \tilde{G}_c} \quad (\text{S14})$$

$$\tilde{K}_c = \tilde{K}_m + \frac{V_f\tilde{K}_m(\tilde{K}_f - \tilde{K}_m)}{\tilde{K}_m + \beta_2(1-V_f)(\tilde{K}_f - \tilde{K}_m)} \quad (\text{S15})$$

$$\tilde{G}_c = \tilde{G}_m + \frac{V_f\tilde{G}_m(\tilde{G}_f - \tilde{G}_m)}{\tilde{G}_m + \beta_1(1-V_f)(\tilde{G}_f - \tilde{G}_m)} \quad (\text{S16})$$

where $\beta_1 = \frac{2(4-5\nu_m)}{15(1-\nu_m)}$, $\beta_2 = 3-5\beta_1$, E is the Young's modulus, \tilde{K} and \tilde{G} denote the bulk modulus and the shear modulus, ν is the Poisson's ratio, V_f is the filler volume fraction, and the subscripts c, f, m refer to the composite, the filler, and the resin matrix, respectively.

Halpin-Tsai model for composite modulus prediction [s21]:

$$E_c = \frac{E_m \left(1 + 2 \frac{E_f - E_m}{E_f + 2E_m} V_f \right)}{1 - \frac{E_f - E_m}{E_f + 2E_m} V_f} \quad (\text{S17})$$

By adapting the relevant parameters of the subject nanocomposites ($E_m = 2.4$ GPa, $\nu_m = 0.35$, $E_f = 70$ GPa for silica, and $\nu_f = 0.17$) into Equation S14-S17, comparisons between predicted and measured elastic modulus are shown in Figure S2a. Both Mori-Tanaka and Halpin-Tsai models underestimate the effective modulus of the nanocomposites compared with the experimental results particularly for those with higher filler content (also applies to the PUA/Fe₃O₄@SiO₂ system studied, results not shown here). These discrepancies may arise from the fact that the models over-simplify the filler-matrix and filler-filler interactions and completely neglect the contribution of the magnetic cores to the overall reinforcing effect of the nanofillers. Developing a more sophisticated model containing multiple phases (e.g. magnetic core, silica shell, resin matrix, core-shell interphase, and filler-matrix interphase) would be beneficial to better understanding the reinforcing mechanisms of complex nanocomposite systems such as the ones studied here; however, this topic is beyond the scope of the present study.

Text 3. Calculation of critical aspect ratio (AR) of micropillars without involving lateral collapse.

Based on a marginal energy balance between stored elastic energy and surface energy, Glassmaker and coauthors derived a theoretical model to predict the maximum height (h_{\max}) of polymeric pillars/fibers that are not subjected to lateral collapse ^[s22]:

$$h_{\max} = \left(\frac{\pi^4 E r}{2^{11} \gamma (1 - \nu^2)} \right)^{1/12} \times \left(\frac{12 E r^3 (d/2)^2}{\gamma} \right)^{1/4} \quad (\text{S18})$$

where E , r , γ , ν , and d are respectively the elastic modulus, radius, surface energy, Poisson's ratio, and center-to-center distance of the round pillars. By adapting all the experimental

parameters for the polyurethane acrylate (PUA) pillars studied into Equation S18, *i.e.* $E = 20$ MPa, $r = 1.25 \mu\text{m}$, $\gamma = 40 \text{ mJ/m}^2$, $\nu = 0.48$, and $d = 6 \mu\text{m}$, h_{max} for the PUA micro-pillars is calculated to be $24.5 \mu\text{m}$. In other words, the maximum AR of the micro-pillars that pure PUA can achieve is $24.5/2.5 = 9.8$, which is fairly close to the experimentally observed AR of 8 for the compliant pillars (CPs) but lower than the AR of 12 that the functional gradient pillars (FGPs) achieved. It is interesting to note that by modifying the value of elastic modulus into 65 MPa (*i.e.* for the stiff pillars according to Figure 4d) and assuming all other parameters the same, h_{max} is calculated to be $\sim 36.2 \mu\text{m}$ corresponding to an AR of 14.5. This agrees with what is expected: pillars made of stiffer materials are less prone to lateral collapse.

Text 4. Derivation of cantilever beam deflections with uniform and functional gradient distribution of elastic modulus.

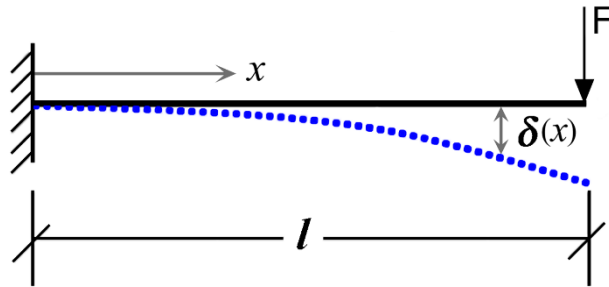


Figure S21. Schematic of cantilever beam subjected to a concentrated force at the free end.

Considering a cantilever beam with a concentrated force F applied at the free end as schematically shown in Figure S21, the fundamental equation governing the beam deflection (δ) is a second-order differential equation according to Euler-Bernoulli beam theory ^[s23]:

$$\frac{d^2 \delta}{dx^2} = \frac{M(x)}{E(x)I(x)} \quad (\text{S19})$$

assuming a high aspect ratio and small deformation of the beam, where $M(x)$, $E(x)$, and $I(x)$ are respectively the bending moment, elastic modulus, and moment of inertia of the beam at position x . For the round beams (pillars) considered in this study, $I(x) \equiv \pi d^4 / 64$ where d is

the diameter of the beam. The bending moment $M(x)$ can be easily determined as:

$$M(x) = -F(l - x) \quad (\text{S20})$$

where l is the length of the beam. Therefore, deflection of beam with uniform elastic modulus (*i.e.* $E(x) \equiv E$) can be obtained by solving Equation S19 combined with Equation S20 and

boundary conditions of $\delta = 0$ and $\frac{d\delta}{dx} = 0$ for $x = 0$:

$$\delta(x) = -\frac{Fx^2}{6EI}(3l - x) \quad (\text{S21})$$

For beam with functional gradient distribution of elastic modulus, the deflection can also be obtained by solving the differential equation incorporated with specific expression of $E(x)$ combined with Equation S20 and the same boundary conditions specified above. Considering the simplest linear transition of the elastic modulus along the beam:

$$E(x) = E_2 - \frac{E_2 - E_1}{l}x = E_2 - sx \quad (\text{S22})$$

where E_1 and E_2 are respectively the elastic modulus of the free and fixed end of the beam and $s = (E_2 - E_1)/l$ is the slope of the transition, the beam deflection (δ^*) can be derived as:

$$\delta^*(x) = -\frac{FE_1}{Is^3}(E_2 - sx)\ln(E_2 - sx) - \frac{F}{2Is}x^2 + \frac{FE_1(1 + \ln(E_2))}{Is^2}x - \frac{FE_1E_2 \ln(E_2)}{Is^3} \quad (\text{S23})$$

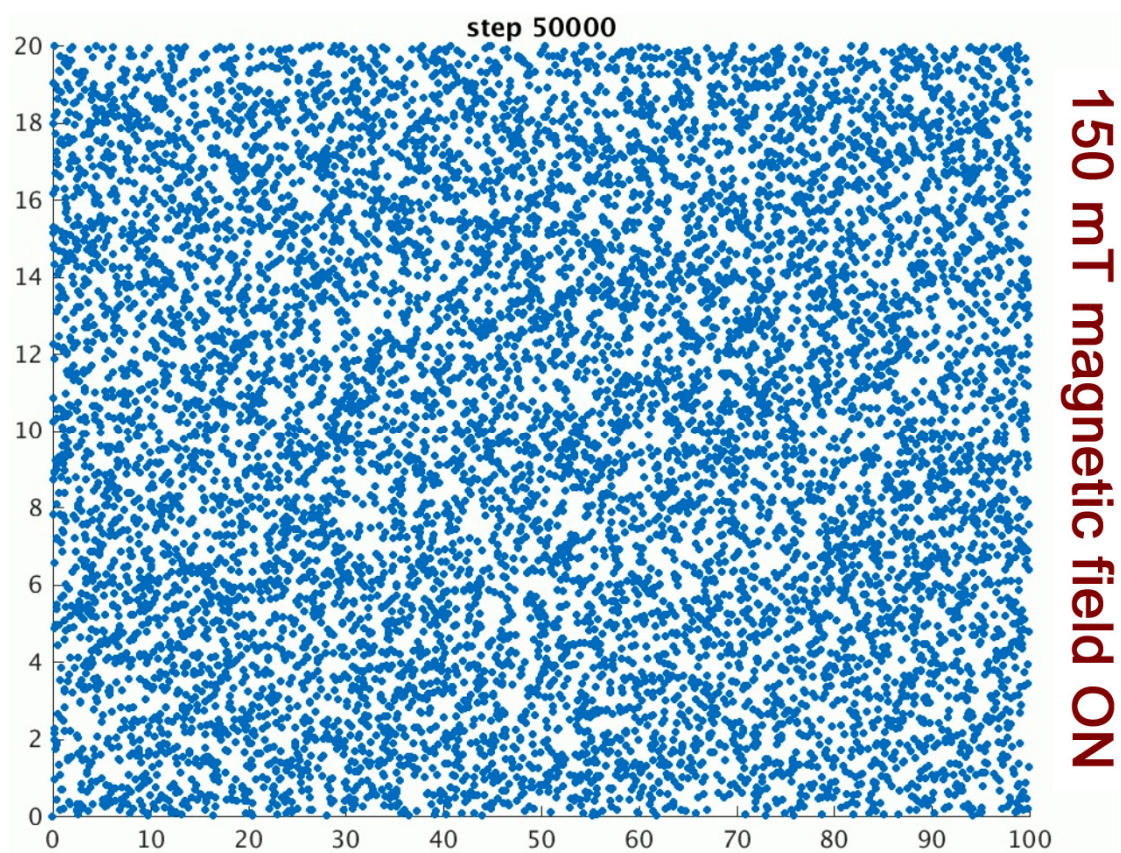
By adapting the relevant experimental data into Equations S21 and S23, the normalized deformations of the CP/SP and FGP are superimposed and compared in Figure S20b with the tip deflections scaled to the same magnitude.

Supplementary References

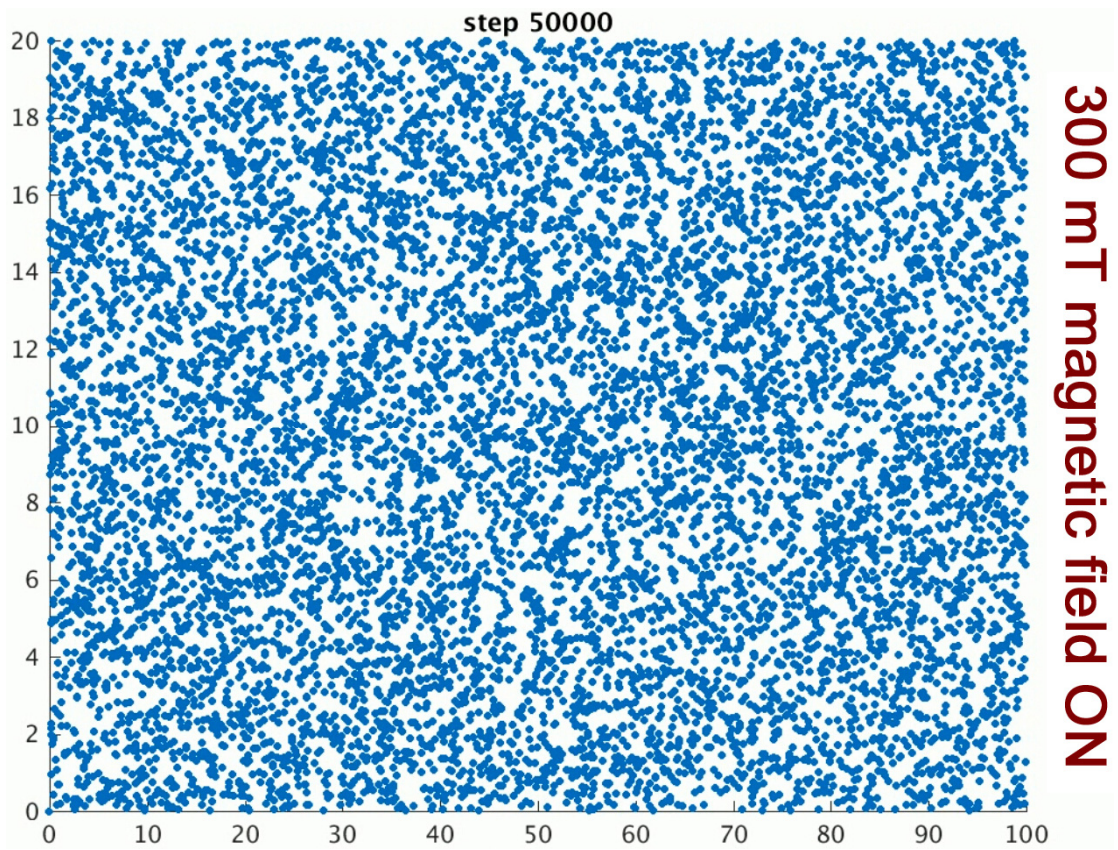
- [s1] J. Park, K. An, Y. Hwang, J.-G. Park, H.-J. Noh, J.-Y. Kim, J.-H. Park, N.-M. Hwang, T. Hyeon, *Nat. Mater.*, 2004, **3**, 891.
- [s2] W.-Y. Rho, H.-M. Kim, S. Kyeong, Y.-L. Kang, D.-H. Kim, H. Kang, C. Jeong, D.-E. Kim, Y.-S. Lee, B.-H. Jun, *J. Ind. Eng. Chem.*, 2014, **20**, 2646
- [s3] W. Stöber, A. Fink, E. Bohn, *J. Colloid. Interf. Sci.*, 1968, **26**, 62.
- [s4] Z. Wang, F. A. Landis, A. A. M. Giuseppetti, S. Lin-Gibson, M. Y. M. Chiang, *Dent. Mater.*, 2014, **30**, 1316.
- [s5] D. Shilo, H. Drezner, A. Dorogoy, *Phys. Rev. Lett.*, 2008, **100**, 035505.
- [s6] C. S. Pfeifer, N. D. Wilson, Z. R. Shelton, J. W. Stansbury, *Polymer*, 2011, **52**, 3295.
- [s7] Z. Wang, P. Gu, X. Wu, H. Zhang, Z. Zhang, M. Y. M. Chiang, *Compos. Sci. Technol.*, 2013, **79**, 49.
- [s8] Z. Wang, P. Gu, X. Wu, *Soft Matter*, 2014, **10**, 3301.
- [s9] J. W. Stansbury, S. H. Dickens, *Dent. Mater.*, 2001, **17**, 71.
- [s10] Z. Wang, M. Y. M. Chiang, *Dent. Mater.*, 2016, **32**, 551.
- [s11] T. Nardi, M. Sangermano, Y. Leterrier, P. Allia, P. Tiberto, J.-A. E. Månson, *Polymer*, 2013, **54**, 4472.
- [s12] R. Libanori, R. M. Erb, A. Reiser, H. Le Ferrand, M. J. Süess, R. Spolenak, A. R. Studart, *Nat. Commun.*, 2012, **3**, 1265.
- [s13] R. R. Gallagher, M. Balooch, G. Balooch, R. S. Wilson, S. J. Marshall, G. W. Marshall, *J. Dent. Biomech.*, 2010, **2010**, 256903.
- [s14] A. Barani, M. B. Bush, B. R. Lawn, *J. Mech. Behav. Biomed. Mater.*, 2012, **15**, 121.
- [s15] E. P. Furlani, K. C. Ng, *Phys. Rev. E*, 2008, **77**, 061914.
- [s16] E. P. Furlani, K. C. Ng, *Phys. Rev. E*, 2006, **73**, 061919.
- [s17] E. P. Furlani, *Permanent magnet and electromechanical devices: Materials, Analysis and Applications*, Academic Press, New York, USA 2001, pp 25-129.

- [s18] E. P. Furlani, X. Xue, *Microfluid. Nanofluid.*, 2012, **13**, 589.
- [s19] S. Y. Fu, X. Q. Feng, B. Lauke, Y. W. Mai, *Composites: Part B*, 2008, **39**, 933.
- [s20] T. Mori, K. Tanaka, *Acta Metall.*, 1973, **21**, 571.
- [s21] J. C. Halpin, J. L. Kardos, *Polym Eng Sci*, 1976, **16**, 344.
- [s22] N. J. Glassmaker, A. Jagota, C.-Y. Hui, J. Kim, *J R Soc Interface*, 2004, **1**, 23.
- [s23] S. P. Timoshenko, J. N. Goodier, *Theory of elasticity. 3rd ed*, McGraw-Hill Book Company, New York, USA 1970, pp. 41-46.

Supplementary Movies



Movie S1. Schematic movie of the migration process of magnetic nanoparticles in viscous medium ($10\ \mu\text{m} \times 2\ \mu\text{m}$ region) under an applied magnetic field of 150 mT.



Movie S2. Schematic movie of the migration process of magnetic nanoparticles in viscous medium ($10 \mu\text{m} \times 2 \mu\text{m}$ region) under an applied magnetic field of 300 mT.